Offset Charge Dependence of Measurement-Induced Transitions in Transmons

Mathieu Féchant,[1,*] Marie Frédérique Dumas,[2,†] Denis Bénâtre,[1] Nicolas Gosling,[1] Philipp Lenhard,[1] Martin Spiecker,[1] Wolfgang Wernsdorfer,[1,3] Benjamin D'Anjou,[2] Alexandre Blais,[2,4] and Ioan M. Pop[1,3,5,‡]

[1] *IQMT, Karlsruhe Institute of Technology, 76131 Karlsruhe, Germany*
[2] *Institut Quantique and Département de Physique, Université de Sherbrooke, Sherbrooke J1K 2R1 QC, Canada*
[3] *PHI, Karlsruhe Institute of Technology, 76131 Karlsruhe, Germany*
[4] *CIFAR, Toronto, M5G 1M1 Ontario, Canada*
[5] *Physics Institute 1, Stuttgart University, 70569 Stuttgart, Germany*

(Dated: May 2, 2025)

A key challenge in achieving scalable fault tolerance in superconducting quantum processors is readout fidelity, which lags behind one- and two-qubit gate fidelity. A major limitation in improving qubit readout is measurement-induced transitions, also referred to as qubit ionization, caused by multiphoton qubit-resonator excitation occurring at specific photon numbers. Since ionization can involve highly excited states, it has been predicted that in transmons—the most widely used superconducting qubit—the photon number at which measurement-induced transitions occur is gate charge dependent. This dependence is expected to persist deep in the transmon regime where the qubit frequency is gate charge insensitive. We experimentally confirm this prediction by characterizing measurement-induced transitions with increasing resonator photon population while actively stabilizing the transmon's gate charge. Furthermore, because highly excited states are involved, achieving quantitative agreement between theory and experiment requires accounting for higher-order harmonics in the transmon Hamiltonian.

Circuit quantum electrodynamics (cQED) with transmon qubits is a leading platform for quantum information processing with superconducting circuits, enabling dispersive qubit readout via coupling to a readout microwave resonator [1–3]. Impressive progress has been achieved towards high-fidelity and quantum nondemolition (QND) qubit readout in this architecture, notably thanks to the development of amplifiers operating near the quantum limit [4–7] and to optimization of the system parameters [8–14]. A key tenet of the dispersive readout is that increasing the number of photons probing the readout resonator should improve the signal-to-noise ratio (SNR) while preserving QND [1]. However, it is experimentally observed that increasing the photon number leads to unwanted qubit transitions, thereby negating the benefits of using strong readout drives [9, 15–18]. This limits the rate of information extraction, creating a bottleneck for error correction in superconducting quantum processors.

Measurement-induced transitions outside of the qubit computational subspace, into high-energy levels of the transmon, have been attributed to multiphoton resonances occurring at specific intracavity photon numbers [16]. This observation has motivated theoretical studies that have led to a framework for understanding this phenomenon—referred to as measurement-induced transitions (MIST) and ionization in the literature—with predictions that are in good agreement with experimental results [16, 18–22]. Crucially, because they involve high-energy states of the transmon, these resonances, and therefore the critical photon number where ionization occurs, have been predicted to be gate-charge dependent [20, 22]. This observation stands in contrast to the transmon's 0-1 transition frequency whose gate-charge dependence is exponentially suppressed with increasing ratio of the qubit's Josephson energy E_J to charging energy E_C [3]. Moreover, because they affect high-energy states, higher-order harmonics of the transmon's Hamiltonian [23] are expected to influence its ionization.

In this work, we present experimental observations confirming the role of gate charge and higher-order harmonics on measurement-induced state transitions. To this end, we measure the impact of the resonator photon population on the qubit state as a function of the average photon number $\bar{n}_r$ and of the qubit frequency ω_{01}, for two transmons of different E_J/E_C ratios. A previous experiment indirectly probed the gate-charge dependence of ionization by observing shot-to-shot variations in the critical photon number, variations that were attributed to fluctuations in the gate charge [18]. Here, the gate charge is actively monitored and stabilized, allowing us to directly confirm the theoretical model discussed in Ref. [22]. This understanding allows us to identify robust regions for readout as a function of n_g, and will inform future qubit calibrations, optimal control, and design strategies.

We use a standard cQED setup consisting of a flux tunable transmon coupled to a readout resonator measured in reflection, see Fig. 1(a). The transmon is capacitively coupled to a line which allows microwave drive and dc charge bias. We apply a readout drive at the resonator input port, loading $\bar{n}_r$ photons. The reflected signal undergoes amplification and we report the mea-

* mathieu.fechant@kit.edu
† Marie.Frederique.Dumas@USherbrooke.ca
‡ ioan.pop@kit.edu

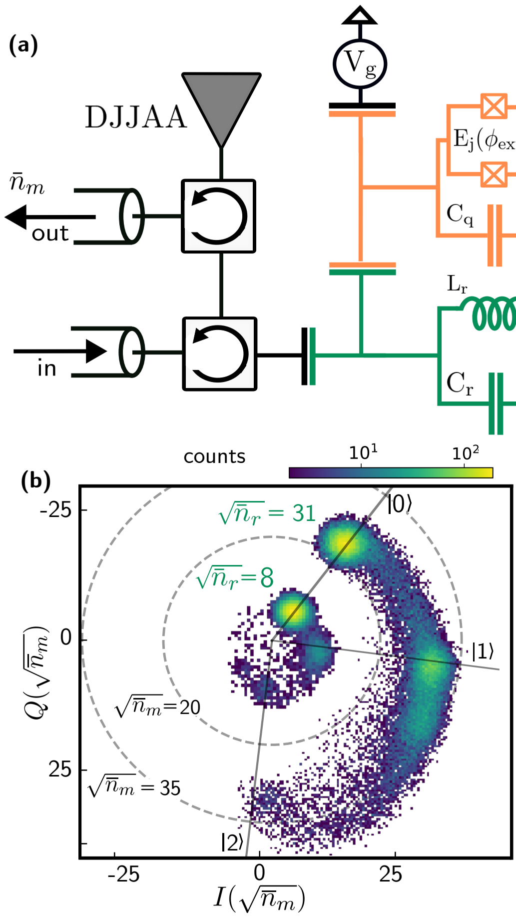

Figure 1. **Dispersive readout.** **(a)** Schematics of a qubit-resonator setup with charge control. The magnetic flux (ϕ_{ext}) tunable transmon (orange) is capacitively coupled to a readout resonator (green) which is measured in reflection through a line with a DJJAA amplifier [25]; see Appendix A for full experimental setup. The qubit is capacitively coupled to a line that allows changing the charge offset n_g. **(b)** Example of a 2D scatter plot of the dispersive measurement outcomes of transmon A, distributed in the IQ quadratures in units of measured photons $\sqrt{\bar{n}_m}$. We continuously pump the readout resonator at $\omega_d/2\pi = 6.119\,72\,\text{GHz}$ and integrate the output every 2 μs. We show the resulting histograms for two different experiments using two different resonator photon numbers, $\sqrt{\bar{n}_r} = 8$ and $\sqrt{\bar{n}_r} = 31$.

sured I and Q quadratures, see Fig. 1(b). Here and below, this is reported in units of the measurement photon number $\bar{n}_m = \bar{n}_r \kappa T_m/4$ during the integration time T_m [24], where κ is the resonator damping rate. The measured values cluster around several IQ coordinates, each corresponding to a transmon state. Deviations from non-QND behavior are evident from the appearance of clusters away from the one corresponding to the initial qubit state, here $|0\rangle$.

To characterize the measurement-induced transitions as a function of external flux and gate charge offset we first use a device (device A) with a readout res-

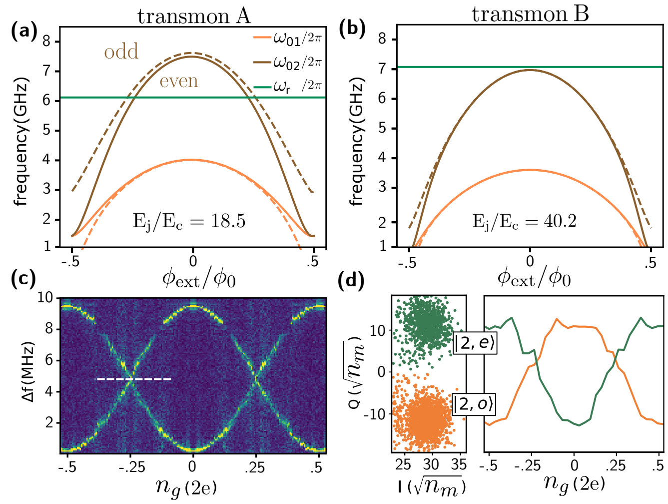

Figure 2. **Flux and Charge Dependence.** **(a,b)** Flux dependence of the 0-1 and 0-2 transmon transitions for device A ($E_J/E_C = 18.5$) and device B ($E_J/E_C = 40.2$) at zero gate charge $n_g = 0$. Energy levels are shown for both even parity states (full lines) and odd parity states (dashed lines) assuming symmetric junctions . **(c)** Charge stabilized dependence of the Fourier transform of a Ramsey interference experiment performed at 3.9965 GHz on device A. Δf giving the frequency difference to the ramsey pulse. The average $\bar{f}_{01}$ at 3.9992 GHz is indicated with a dashed line. **(d)** Left panel: IQ clouds corresponding to state $|2, \text{o}\rangle$ and $|2, \text{e}\rangle$ in units of $\sqrt{\bar{n}_m}$ after a 4 μs pulse for device B. We observe direct dispersive readout of the parity [29]. Right panel: Imaginary part for each distribution corresponding to the even and odd second transmon excited state over one charge period.

onator frequency $\omega_r/2\pi = 6.12\,\text{GHz}$ and decay rate $\kappa/2\pi = 2.6\,\text{MHz}$. The resonator is coupled with strength $g/2\pi = 13\,\text{MHz}$ to a transmon qubit of charging energy $E_C/2\pi = 365\,\text{MHz}$ and maximum Josephson energy $E_J/2\pi = 6.71\,\text{GHz}$ at zero flux bias $\phi_{\text{ext}} = 0$. With a maximum E_J/E_C ratio of ~ 18.5, this device is in the shallow transmon regime with $\sim 9\,\text{MHz}$ charge dispersion of the 0-1 transition. Figure 2(a) shows the flux dependence of the transmon's transition frequencies between the ground state and the first two excited states. To stabilize the charge offset, we measure Ramsey fringes of the 0-1 transition as a function of the gate charge, revealing two sinusoids of periodicity $2e$; see Fig. 2(c) [26, 27]. The two measured frequencies result from random quasiparticle tunneling events shifting the response by $1e$; see also the full and dashed lines in Fig. 2(a) labeled even and odd, respectively [28]. We calibrate n_g by measuring the frequency difference at multiple charge offsets, a process which takes about 10 s. By repeatedly performing this active monitoring, we achieve control over n_g with 2 % precision.

To confirm the importance of gate charge on ionization deeper in the transmon regime, where the computational states have a much weaker dependence on gate charge, we also measure a device (device B) with a charg-

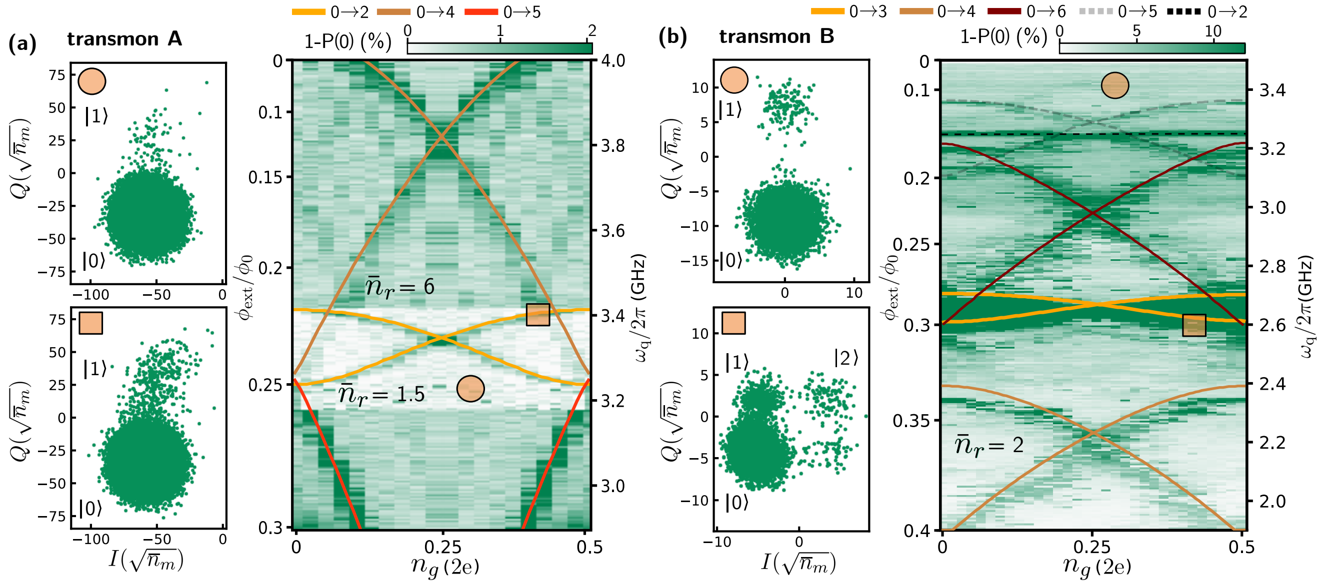

Figure 3. **Probability $1-P(0)$ to find the transmon in an excited state vs. flux and charge offset.** **(a)** For device A, we continuously populate the resonator with $\bar{n}_r \approx 6$ photons at frequency $\omega_d/2\pi = 6.119\,72\,\mathrm{GHz}$ and integrate over 25 μs. In the central part of the plot we lower the photon number to $\bar{n}_r \approx 1.5$ to reduce the width of the features. **(b)** For device B, we stroboscopically pump the resonator with $\bar{n}_r \approx 2$ photons at $\omega_d/2\pi = 7.0535\,\mathrm{GHz}$ with a 2 μs pulse every 3 μs. In both panels, the qubit frequency corresponding to $\phi_{\rm ext}$ and $n_g = 0$ is indicated by the right axis. We show as side panels selected IQ clouds for specific values of flux and gate charge to highlight the contrast between negligible (circle) and significant (square) leakage. The photon number $\bar{n}_r$ is calibrated with an ac-Stark shift experiment performed at low power. The multiphoton resonance conditions $\omega_{0j} = n\omega_d$, labeled as $0 \to j$, are plotted on top of the experimental results (orange-red lines). The remaining discrepancies $\lesssim 100\,\mathrm{MHz}$ are consistent with frequency shifts expected from sources that are presently not accounted for in our model, such as junction asymmetry. The dashed lines indicate the theory for inelastic scattering with a spurious mode of frequency 0.78 GHz.

ing energy $E_C/2\pi = 217\,\mathrm{MHz}$ and maximum Josephson energy $E_J/2\pi = 8.72\,\mathrm{GHz}$ at zero flux bias $\phi_{\rm ext} = 0$, yielding $E_J(\phi_{\rm ext})/E_C \leq 40.2$; see Fig. 2(b). This qubit is coupled with strength $g/2\pi = 186.5\,\mathrm{MHz}$ to a readout resonator of frequency $\omega_r/2\pi = 7.05\,\mathrm{GHz}$ and decay rate $\kappa/2\pi = 0.92\,\mathrm{MHz}$. At this large E_J/E_C ratio, the charge dispersion of $\sim 50\,\mathrm{kHz}$ is too small to be resolved through Ramsey interferometry. To calibrate the gate charge, we instead rely on the strong hybridization of the readout mode with the charge-sensitive transmon state $|2\rangle$ [29]. As shown in Fig. 2(d), by monitoring the charge offset imprinted on the resonator's dispersive shift for state $|2\rangle$, we calibrate n_g with better than 5% precision.

To map the measurement-induced transitions as a function of the qubit control parameters, we monitor the average state of the qubit by probing the response of the resonator with a maximum of $\bar{n}_r \sim 6$ photons. The resulting probability to find the transmon in a state other than $|0\rangle$, $1-P(0)$, is reported in Fig. 3. For both devices we observe flux- and gate-charge-dependent features symmetric about $n_g = 0.25$ due to frequent parity switching induced by quasiparticle tunneling events. These features correspond to regions where transitions out of the ground state are more pronounced. The response of the resonator in the IQ plane on top of (square) and away from (circle) one of these features are shown as side panels. Here, the moderate value of $\bar{n}_r \lesssim 6$ is chosen to avoid excessive broadening of the gate-charge-dependent features in the main panels and, as discussed below, to limit the qubit's ac-Stark shift.

To understand the origin of these features, we model the measurement-induced transitions by treating the field in the readout resonator as an effective classical drive on the transmon. This is described by the time-dependent Hamiltonian [20, 22, 30]

$$\hat{H}(t) = \hat{H}_t + \varepsilon_t(t)\cos(\omega_d t)\,\hat{n}_t, \tag{1}$$

where $\hat{H}_t$ is the undriven transmon Hamiltonian. Here we account for higher-order harmonics of the potential such that $\hat{H}_t$ reads [23]

$$\hat{H}_t = 4E_C(\hat{n}_t - n_g)^2 - \sum_{m\geq 1} E_{Jm}\cos(m\hat{\varphi}_t). \tag{2}$$

In this expression, $\hat{n}_t$ and $\hat{\varphi}_t$ are the transmon charge and phase operators, respectively, $\omega_d \approx \omega_r$ is the drive frequency, and $\varepsilon_t(t) = 2g\sqrt{\bar{n}_r(t)}$ is the effective time-dependent drive amplitude; see Appendix B. The charging energy E_C and the Josephson energies E_{Jm} are fitted to independently measured transition frequencies at different values of n_g; see Appendix C. Higher harmonics are fitted only for device B, as device A's sharp n_g dependence of critical photon numbers is not probed.

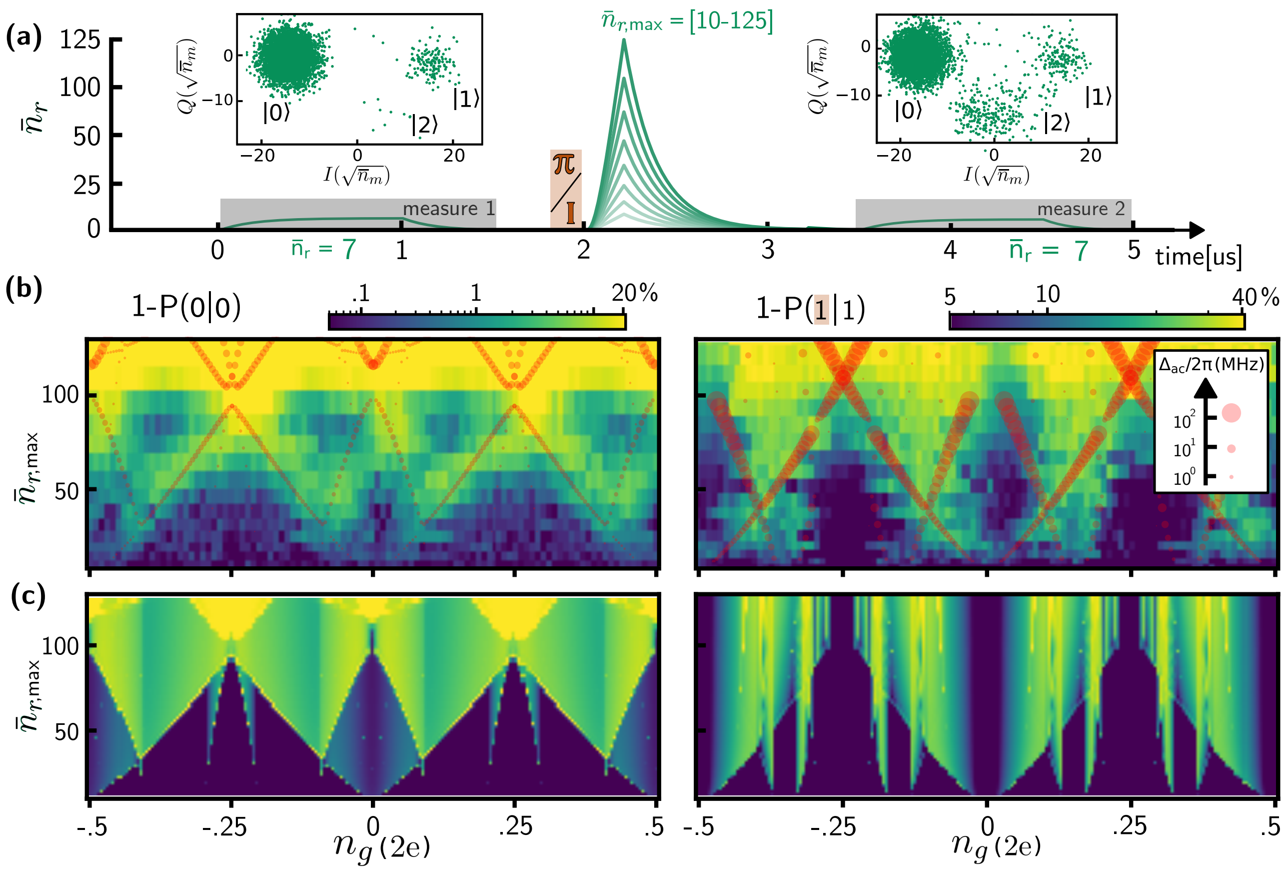

Figure 4. **Probability of leaving the initial state for device B. (a)** Experimental pulse sequence. We apply a high-power 200 ns readout pulse with variable amplitude ($\bar{n}_{r,\max} \in [10, 125]$), straddled by two low-power 1 μs readout pulses ($\bar{n}_{r,\max} = 7$) for high-fidelity preparation and readout. An optional π-pulse enables preparation of the excited state. All pulses have frequency $\omega_d/2\pi = 7.0535\,\mathrm{GHz}$. The insets show the IQ data for the preparation and final measurements for $\bar{n}_{r,\max} = 50$ and $n_g = 0$. **(b)** Measurement-induced transition probability as a function of gate charge and maximum average photon number in the resonator when initializing the qubit in the ground state (left) or excited state (right). The photon number at higher powers is calibrated by extrapolating a nonlinear semiclassical model of resonator dynamics; see Appendix E. Red circles indicate the positions of avoided crossings in the Floquet quasienergy spectrum. The dot area is proportional to the gap size Δ_{ac}. (c) Numerical simulation of the experiment from the semiclassical time dynamics. The color bars are the same for theory and experiment.

At low photon number $\bar{n}_r$, the qubit's ac-Stark shift is small and, following Eq. (1), we expect multiphoton transitions to occur when $\omega_{ij} \approx n\omega_d$, where $\omega_{ij} = \omega_j - \omega_i$ with ω_i a bare eigenfrequency of $\hat{H}_t$ and n an integer corresponding to the number of readout photons involved in the process. The lines shown in Fig. 3 indicate the predicted resonance conditions assuming no junction asymetry for selected $i \to j$ transitions, as specified in the legend, and show remarkable agreement with the measured leakage probability. For device A, the features close to $\phi_{\mathrm{ext}}/\phi_0 = 0.23$ (light orange lines) correspond to a $0 \to 2$ transition involving a single drive photon, $\omega_{02} \approx \omega_d$; see Fig. 2(a) where this resonance and its charge dispersion is also evident. Because this is a first-order process, non-QND behavior is very pronounced. For this reason, a smaller resonator photon number ($\bar{n}_r = 1.5$) is used in the vicinity of this resonance compared to the rest of the plot ($\bar{n}_r = 6$). For device B, a similar first-order resonance between the transmon states 0 and 3 with strong non-QND behavior is also observed (light orange lines).

That device also shows a large leakage probability around $\omega_{01}/2\pi = 3.26\,\mathrm{GHz}$ for all values of n_g that does not directly match a $0 \to j$ multiphoton transition. This leakage can be explained by inelastic scattering of readout photons via a spurious mode at $\omega_s/2\pi = 0.78\,\mathrm{GHz}$ in the qubit environment [31–34], for which the resonance condition $\omega_{02}+\omega_s \approx \omega_d$ is satisfied (black dashed line). Assuming the existence of a mode at this frequency also predicts the increased leakage observed around $\omega_{05}+\omega_s \approx 2\omega_d$ (gray dashed line). Away from the resonances, the residual transition probability shows a trend towards a more QND behavior as the qubit-resonator detuning increases, consistent with recent results [35].

At larger resonator photon number, the transmon levels can be significantly ac-Stark shifted such that the multiphoton resonance conditions now involve the transmon frequencies dressed by the drive rather than the bare ones [16, 21, 22]. To measure ionization in this situation, we follow the measurement protocol shown in Fig. 4(a). We first prepare the transmon of device B, operated at the flux sweet spot, in state $|0\rangle$ by postselecting on the result of a first low-power measurement ($\bar{n}_r \sim 7$). In half the realizations, we then apply a π-pulse to prepare the excited state $|1\rangle$. Next, we populate the resonator with up to $\bar{n}_r = 125$ photons. Finally, we assess the non-QND character of this strong drive by performing a second QND measurement to determine the qubit's final state. We assume that the low power pulses are QND compared to the high power pulse. As can be seen by comparing the two insets in Fig. 4(a), the strong drive results in population transfer to excited states.

Figure 4(b) shows the measured population transfer when starting in $|0\rangle$ (left) and $|1\rangle$ (right) as a function of the gate charge and resonator photon number. We observe a rich charge-dependent structure, with sharp increases in non-QNDness at specific n_g-dependent photon numbers.

To obtain a quantitative understanding of these observations, we use Floquet theory to compute the quasienergy spectrum of Eq. (1) as a function of the amplitude of the effective drive ε_t on the qubit; see Appendix D. From these quasienergies, which encapsulate the drive-induced ac-Stark shifts, we identify avoided crossings corresponding to multiphoton resonances, here shown as red dots in Fig. 4(b) [22]. The gap Δ_{ac} at the avoided crossing, which is indicated by the area of the dots, increases with the amplitude of the effective drive, reflecting a stronger hybridization of the transmon with the drive. Importantly, the quantitative agreement between experimental results and the Floquet calculations seen in Fig. 4(b) is only obtained when including higher-order harmonics up to $m = 3$; see Appendix H. This is because the observed transitions involve highly excited states that lie above the top of the cosine potential well. These states are strongly sensitive to the presence of higher-order harmonics as well as the gate charge; see Appendix G. However, as discussed in more detail in Appendix H, this dependence of the critical photon number on higher-order harmonics does not provide sufficient information to determine the specific origin of these harmonics in our experiment.

We note that in Fig. 4(b), the QNDness does not decrease monotonically with increasing $\bar{n}_{r,\max}$; in some regions above a resonance, higher QNDness is observed. This behavior, consistent with the findings of Sank *et al.* [16], arises from Landau-Zener transitions that occur as the system sweeps through multiphoton resonances [19, 22]. The resulting non-QNDness thus depends on both the rate at which a given resonance is traversed and the size of the associated energy gap Δ_{ac}. Because larger $\bar{n}_{r,\max}$ are associated with a faster crossing of resonances during the transients, a resonance that leads to non-QND behavior at small $\bar{n}_{r,\max}$ may no longer contribute at larger values. To model these complex dynamics, we solve the Schrödinger equation with the Hamiltonian of Eq. (1) and following the same protocol as the experiment; see Appendix F. The resulting theoretical transition probabilities are presented in Fig. 4(c). Crucially, the numerical calculations account for the rise and fall of the resonator population (cf. Appendix E), which results in some resonances being traversed twice. Despite the simplicity of the model, we find remarkable agreement between the experimental and theoretical results, without the use of adjustable parameters.

In summary, we have directly probed the gate charge dependence of measurement-induced transitions in transmons, confirming recent theoretical predictions [20, 22]. This was made possible by active stabilization of the gate charge. A key finding is that achieving quantitative agreement between experiment and theory requires accounting for higher-order harmonics of the transmon Hamiltonian. Additionally, our results show that the ring-up and ring-down transients influence measurement-induced state transitions. Our findings suggest that charge stabilization can help avoid regions that are most susceptible to unwanted multiphoton transitions, therefore enabling a path towards higher fidelity QND readout. These results are broadly applicable to other nonlinear driven superconducting circuits dispersive readout, such as parametric gates and couplers, qubit reset protocols, and quantum state stabilization schemes.

ACKNOWLEDGEMENTS

We are grateful to Dennis Willsch, Madita Willsch, Alexandru Petrescu and Dennis Rieger for stimulating discussions. We thank L. Radtke and S. Diewald for technical assistance. This work was financed by the German Ministry of Education and Research (BMBF) within project QSolid (FKZ:13N16151). D.B. acknowledges funding from the Horizon Europe program via Project No. 101113946 OpenSuperQPlus100. N.G. and M.S. acknowledge funding from the German Ministry of Education and Research (BMBF) within project GEQCOS (FKZ: 13N15683). Facilities use was supported by the KIT Nanostructure Service Laboratory. We acknowledge the measurement software framework qKit. MFD, BD and AB were supported by NSERC, the Ministère de l'Économie et de l'Innovation du Québec, the Canada First Research Excellence Fund, and the U.S. Department of Energy, Office of Science, National Quantum Information Science Research Centers, Quantum Systems Accelerator.

[1] A. Blais, R.-S. Huang, A. Wallraff, S. M. Girvin, and R. J. Schoelkopf, Cavity quantum electrodynamics for superconducting electrical circuits: An architecture for quantum computation, Phys. Rev. A **69**, 062320 (2004).

[2] A. Wallraff, D. I. Schuster, A. Blais, L. Frunzio, J. Majer, M. H. Devoret, S. M. Girvin, and R. J. Schoelkopf, Approaching unit visibility for control of a superconducting qubit with dispersive readout, Phys. Rev. Lett. **95**, 060501 (2005).

[3] J. Koch, T. M. Yu, J. Gambetta, A. A. Houck, D. I. Schuster, J. Majer, A. Blais, M. H. Devoret, S. M. Girvin, and R. J. Schoelkopf, Charge-insensitive qubit design derived from the Cooper pair box, Phys. Rev. A **76**, 042319 (2007).

[4] T. Yamamoto, K. Inomata, M. Watanabe, K. Matsuba, T. Miyazaki, W. D. Oliver, Y. Nakamura, and J. S. Tsai, Flux-driven Josephson parametric amplifier, Applied Physics Letters **93**, 042510 (2008).

[5] M. A. Castellanos-Beltran, K. D. Irwin, G. C. Hilton, L. R. Vale, and K. W. Lehnert, Amplification and squeezing of quantum noise with a tunable Josephson metamaterial, Nat Phys **4**, 929 (2008).

[6] R. Vijay, D. H. Slichter, and I. Siddiqi, Observation of quantum jumps in a superconducting artificial atom, Phys. Rev. Lett. **106**, 110502 (2011).

[7] C. Macklin, K. O'Brien, D. Hover, M. E. Schwartz, V. Bolkhovsky, X. Zhang, W. D. Oliver, and I. Siddiqi, A near–quantum-limited Josephson traveling-wave parametric amplifier, Science **350**, 307 (2015).

[8] C. C. Bultink, M. A. Rol, T. E. O'Brien, X. Fu, B. C. S. Dikken, C. Dickel, R. F. L. Vermeulen, J. C. de Sterke, A. Bruno, R. N. Schouten, and L. DiCarlo, Active resonator reset in the nonlinear dispersive regime of circuit qed, Phys. Rev. Appl. **6**, 034008 (2016).

[9] T. Walter, P. Kurpiers, S. Gasparinetti, P. Magnard, A. Potočnik, Y. Salathé, M. Pechal, M. Mondal, M. Oppliger, C. Eichler, and A. Wallraff, Rapid high-fidelity single-shot dispersive readout of superconducting qubits, Phys. Rev. Appl. **7**, 054020 (2017).

[10] I. Takmakov, P. Winkel, F. Foroughi, L. Planat, D. Gusenkova, M. Spiecker, D. Rieger, L. Grünhaupt, A. V. Ustinov, W. Wernsdorfer, I. M. Pop, and N. Roch, Minimizing the Discrimination Time for Quantum States of an Artificial Atom, Phys. Rev. Appl. **15**, 064029 (2021).

[11] Y. Sunada, S. Kono, J. Ilves, S. Tamate, T. Sugiyama, Y. Tabuchi, and Y. Nakamura, Fast Readout and Reset of a Superconducting Qubit Coupled to a Resonator with an Intrinsic Purcell Filter, Phys. Rev. Appl. **17**, 044016 (2022).

[12] F. Swiadek, R. Shillito, P. Magnard, A. Remm, C. Hellings, N. Lacroix, Q. Ficheux, D. C. Zanuz, G. J. Norris, A. Blais, S. Krinner, and A. Wallraff, Enhancing dispersive readout of superconducting qubits through dynamic control of the dispersive shift: Experiment and theory, PRX Quantum **5**, 040326 (2024).

[13] M. Jerger, F. Motzoi, Y. Gao, C. Dickel, L. Buchmann, A. Bengtsson, G. Tancredi, C. W. Warren, J. Bylander, D. DiVincenzo, R. Barends, and P. A. Bushev, Dispersive qubit readout with intrinsic resonator reset (2024), arXiv:2406.04891 [quant-ph].

[14] P. A. Spring, L. Milanovic, Y. Sunada, S. Wang, A. F. van Loo, S. Tamate, and Y. Nakamura, Fast multiplexed superconducting qubit readout with intrinsic purcell filtering (2024), arXiv:2409.04967 [quant-ph].

[15] E. Jeffrey, D. Sank, J. Y. Mutus, T. C. White, J. Kelly, R. Barends, Y. Chen, Z. Chen, B. Chiaro, A. Dunsworth, A. Megrant, P. J. J. O'Malley, C. Neill, P. Roushan, A. Vainsencher, J. Wenner, A. N. Cleland, and J. M. Martinis, Fast Accurate State Measurement with Superconducting Qubits, Phys. Rev. Lett. **112**, 190504 (2014).

[16] D. Sank, Z. Chen, M. Khezri, J. Kelly, R. Barends, B. Campbell, Y. Chen, B. Chiaro, A. Dunsworth, A. Fowler, E. Jeffrey, E. Lucero, A. Megrant, J. Mutus, M. Neeley, C. Neill, P. O'Malley, C. Quintana, P. Roushan, A. Vainsencher, T. White, J. Wenner, A. N. Korotkov, and J. M. Martinis, Measurement-induced state transitions in a superconducting qubit: Beyond the rotating wave approximation, Phys. Rev. Lett. **117**, 190503 (2016).

[17] Z. K. Minev, S. O. Mundhada, S. Shankar, P. Reinhold, R. Gutiérrez-Jáuregui, R. J. Schoelkopf, M. Mirrahimi, H. J. Carmichael, and M. H. Devoret, To catch and reverse a quantum jump mid-flight, Nature **570**, 200 (2019).

[18] M. Khezri, A. Opremcak, Z. Chen, K. C. Miao, M. McEwen, A. Bengtsson, T. White, O. Naaman, D. Sank, A. N. Korotkov, Y. Chen, and V. Smelyanskiy, Measurement-induced state transitions in a superconducting qubit: Within the rotating-wave approximation, Phys. Rev. Appl. **20**, 054008 (2023).

[19] R. Shillito, A. Petrescu, J. Cohen, J. Beall, M. Hauru, M. Ganahl, A. G. Lewis, G. Vidal, and A. Blais, Dynamics of transmon ionization, Phys. Rev. Appl. **18**, 034031 (2022).

[20] J. Cohen, A. Petrescu, R. Shillito, and A. Blais, Reminiscence of classical chaos in driven transmons, PRX Quantum **4**, 020312 (2023).

[21] X. Xiao, J. Venkatraman, R. G. Cortiñas, S. Chowdhury, and M. H. Devoret, A diagrammatic method to compute the effective Hamiltonian of driven nonlinear oscillators (2023), arXiv:2304.13656 [quant-ph].

[22] M. F. Dumas, B. Groleau-Paré, A. McDonald, M. H. Muñoz Arias, C. Lledó, B. D'Anjou, and A. Blais, Measurement-induced transmon ionization, Phys. Rev. X **14**, 041023 (2024).

[23] D. Willsch, D. Rieger, P. Winkel, M. Willsch, C. Dickel, J. Krause, Y. Ando, R. Lescanne, Z. Leghtas, N. T. Bronn, P. Deb, O. Lanes, Z. K. Minev, B. Dennig, S. Geisert, S. Günzler, S. Ihssen, P. Paluch, T. Reisinger, R. Hanna, J. H. Bae, P. Schüffelgen, D. Grützmacher, L. Buimaga-Iarinca, C. Morari, W. Wernsdorfer, D. P. DiVincenzo, K. Michielsen, G. Catelani, and I. M. Pop, Observation of josephson harmonics in tunnel junctions, Nature Physics **20**, 815 (2024).

[24] M. Hatridge, S. Shankar, M. Mirrahimi, F. Schackert, K. Geerlings, T. Brecht, K. M. Sliwa, B. Abdo, L. Frunzio, S. M. Girvin, R. J. Schoelkopf, and M. H. Devoret, Quantum back-action of an individual variable-strength measurement, Science **339**, 178 (2013).

[25] P. Winkel, I. Takmakov, D. Rieger, L. Planat, W. Hasch-Guichard, L. Grünhaupt, N. Maleeva, F. Foroughi,

F. Henriques, K. Borisov, J. Ferrero, A. V. Ustinov, W. Wernsdorfer, N. Roch, and I. M. Pop, Nondegenerate parametric amplifiers based on dispersion-engineered josephson-junction arrays, Phys. Rev. Appl. **13**, 024015 (2020).

[26] K. Serniak, M. Hays, G. de Lange, S. Diamond, S. Shankar, L. D. Burkhart, L. Frunzio, M. Houzet, and M. H. Devoret, Hot non-equilibrium quasiparticles in transmon qubits, Physical Review Letters **121**, 157701 (2018), arXiv:1803.00476 [cond-mat, physics:quant-ph].

[27] D. Ristè, C. C. Bultink, M. J. Tiggelman, R. N. Schouten, K. W. Lehnert, and L. DiCarlo, Millisecond charge-parity fluctuations and induced decoherence in a superconducting transmon qubit, Nature Communications **4**, 10.1038/ncomms2936 (2013).

[28] J. A. Schreier, A. A. Houck, J. Koch, D. I. Schuster, B. R. Johnson, J. M. Chow, J. M. Gambetta, J. Majer, L. Frunzio, M. H. Devoret, S. M. Girvin, and R. J. Schoelkopf, Suppressing charge noise decoherence in superconducting charge qubits, Phys. Rev. B **77**, 180502 (2008).

[29] K. Serniak, S. Diamond, M. Hays, V. Fatemi, S. Shankar, L. Frunzio, R. Schoelkopf, and M. Devoret, Direct Dispersive Monitoring of Charge Parity in Offset-Charge-Sensitive Transmons, Physical Review Applied **12**, 014052 (2019).

[30] C. Lledó, R. Dassonneville, A. Moulinas, J. Cohen, R. Shillito, A. Bienfait, B. Huard, and A. Blais, Cloaking a qubit in a cavity, Nat. Commun. **14**, 6313 (2023).

[31] S. Singh, G. Refael, A. Clerk, and E. Rosenfeld, Impact of josephson junction array modes on fluxonium readout (2025), arXiv:2412.14788 [cond-mat.mes-hall].

[32] A. Bista, M. Thibodeau, K. Nie, K. Chow, B. K. Clark, and A. Kou, Readout-induced leakage of the fluxonium qubit (2025), arXiv:2501.17807 [quant-ph].

[33] B. Hoyau, A. McDonald, B. Varbanov, M. Muños-Arias, and A. Blais, In preparation.

[34] W. Dai, S. Hazra, X. Xiao , J. Venkatraman, Z Wang, P. D Parakh, D. K. Weiss, L. Frunzio M. H. Devoret, Investigating readout-induced state transitions in a multimode josephson circuit, march meeting talk (2025).

[35] P. D. Kurilovich, T. Connolly, C. G. L. Bøttcher, D. K. Weiss, S. Hazra, V. R. Joshi, A. Z. Ding, H. Nho, S. Diamond, V. D. Kurilovich, W. Dai, V. Fatemi, L. Frunzio, L. I. Glazman, and M. H. Devoret, High-frequency readout free from transmon multi-excitation resonances (2025), arXiv:2501.09161 [quant-ph].

[36] N. Maleeva, L. Grünhaupt, T. Klein, F. Levy-Bertrand, O. Dupre, M. Calvo, F. Valenti, P. Winkel, F. Friedrich, W. Wernsdorfer, A. V. Ustinov, H. Rotzinger, A. Monfardini, M. V. Fistul, and I. M. Pop, Circuit quantum electrodynamics of granular aluminum resonators, Nature Communications **9**, 10.1038/s41467-018-06386-9 (2018).

[37] J. Krause, G. Marchegiani, L. Janssen, G. Catelani, Y. Ando, and C. Dickel, Quasiparticle effects in magnetic-field-resilient three-dimensional transmons, Phys. Rev. Appl. **22**, 044063 (2024).

[38] H. Breuer and M. Holthaus, Quantum phases and Landau-Zener transitions in oscillating fields, Phys. Lett. A **140**, 507 (1989).

[39] M. Grifoni and P. Hänggi, Driven quantum tunneling, Phys. Rep. **304**, 229 (1998).

[40] K. Drese and M. Holthaus, Floquet theory for short laser pulses, Eur. Phys. J. D **5**, 119 (1999).

[41] W. D. Oliver, Y. Yu, J. C. Lee, K. K. Berggren, L. S. Levitov, and T. P. Orlando, Mach-Zehnder interferometry in a strongly driven superconducting qubit, Science **310**, 1653 (2005).

[42] S. Shevchenko, S. Ashhab, and F. Nori, Landau–Zener–Stückelberg interferometry, Phys. Rep. **492**, 1 (2010).

[43] T. N. Ikeda, S. Tanaka, and Y. Kayanuma, Floquet-Landau-Zener interferometry: Usefulness of the Floquet theory in pulse-laser-driven systems, Phys. Rev. Res. **4**, 033075 (2022).

[44] J. Gambetta, A. Blais, D. I. Schuster, A. Wallraff, L. Frunzio, J. Majer, M. H. Devoret, S. M. Girvin, and R. J. Schoelkopf, Qubit-photon interactions in a cavity: Measurement-induced dephasing and number splitting, Phys. Rev. A **74**, 042318 (2006).

SUPPLEMENTAL MATERIAL

Appendix A: Measurement setup

Figure 5 shows the setup used for all the qubit measurements. The samples are measured in a copper waveguide setup similar to Ref. [36], which is then encased in a shielding barrel with eccosorb glue on a copper cylinder, an Aluminium cylinder, and a Cryoperm shield. The readout line is connected to the bottom of the waveguide, which acts as a Purcell filter below the cutoff frequency of 6 GHz. There is then a pin closer to the device which is used to drive and offset the qubit. Device A exhibits a strong variation of dephasing time T_2 with gate charge, which is linked to the charge dispersion and noise coming from the qubit drive pin. After shortening the pin and moving the device away from the qubit drive, the measurement reported in Fig. 3 was done such that 2e is around 40 mV and the T_2 value vs gate charge indicates a charge noise of 0.02 in units of 2e. Device B does not exhibit a variation of T_2 with charge but shows an oscillation of 2e for 80 mV. We amplify the signal using a DJJAA amplifier [25] with an amplification between 15 and 20 dB for both devices. The signal is then reamplified at 4K by the HEMT amplifier and at room temperature using an LNF LNF-LNR1_15B_SV amplifier. For device B measurements, a homemade RF filter with a bandwidth of 30 MHz was added to the readout driving line to remove some unwanted sidebands of the drive pulses. The microwave signals are sent and recorded using a Presto machine, a frequency signal generation and analysis platform from Intermodulation Products AB.

Appendix B: Semiclassical model

This section outlines the derivation of Eq. (1). The static transmon-resonator system Hamiltonian is

$$\hat{H}_{tr} = \hat{H}_t + \omega_r \hat{a}^\dagger \hat{a} - ig(\hat{n}_t - n_g)(\hat{a} - \hat{a}^\dagger), \quad \text{(B1)}$$

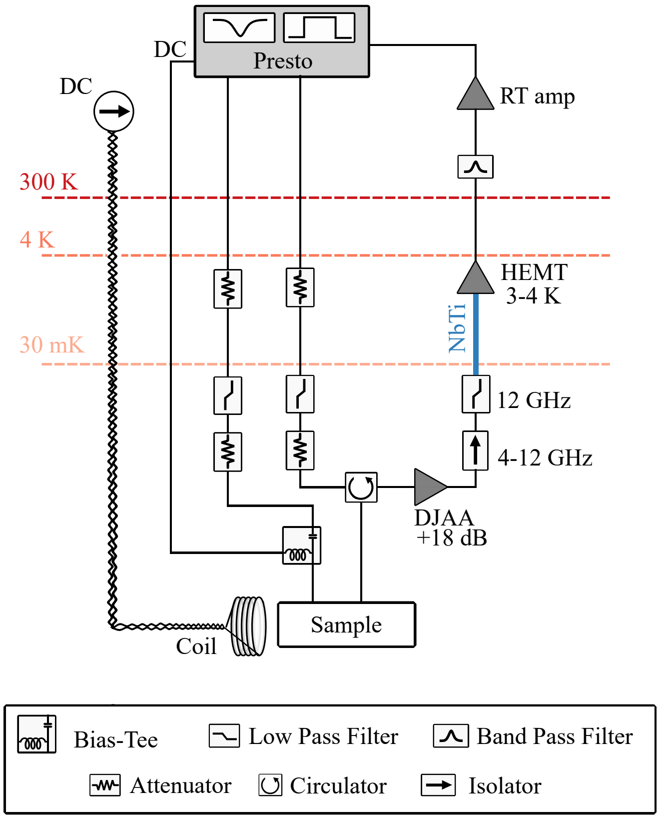

Figure 5. **Experimental setup**

with $\hat{H}_t$ the transmon Hamiltonian given by Eq. (2), $\hat{n}_t$ the transmon charge operator, $\hat{a}$ the annihilation operator of the resonator, ω_r the bare resonator frequency, and g the coupling strength. The system parameters are obtained from spectroscopy as detailed in Appendix C. In the presence of a drive on the resonator, the full Hamiltonian is

$$\hat{H}(t) = \hat{H}_{tr} - i\varepsilon_d \sin(\omega_d t)(\hat{a} - \hat{a}^\dagger), \tag{B2}$$

where ε_d and ω_d are the drive amplitude and frequency. In a frame rotating at frequency ω_d and neglecting the fast-rotating terms, the Hamiltonian is

$$\begin{aligned}\hat{H}(t) =& \hat{H}_t + (\omega_r - \omega_d)\hat{a}^\dagger\hat{a} - ig(\hat{n}_t - n_g)(\hat{a}e^{-i\omega_d t} - \hat{a}^\dagger e^{i\omega_d t}) \\ & - i\varepsilon_d(\hat{a}e^{-i\omega_d t} - \hat{a}^\dagger e^{i\omega_d t}).\end{aligned} \tag{B3}$$

We apply a displacement transformation on the resonator which results in the replacement

$$\hat{a} \to \hat{a} + \alpha(t), \tag{B4}$$

where $\alpha(t)$ is the coherent state amplitude and the remaining $\hat{a}$ on the right-hand-side denotes quantum fluctuations of the resonator. The semiclassical approximation neglects the quantum fluctuations, leading to the driven transmon Hamiltonian

$$\hat{H}(t) = \hat{H}_t + 2g\sqrt{\bar{n}_r(t)}\cos[\omega_d t + \phi(t)](\hat{n}_t - n_g). \tag{B5}$$

Here, $\bar{n}_r(t) = |\alpha(t)|^2$ is the average photon number and $\phi(t)$ is a slowly oscillating phase of the resonator field. Since it varies slowly on the timescale of a resonance crossing, this phase can be neglected—it does not affect the Landau-Zener dynamics responsible for population transfer. Neglecting it also makes Eq. (B5) time-periodic.

In the dispersive readout, the resonator field takes a value $\alpha_i(t)$ that is conditional on the transmon state i. The semiclassical dynamics of $\alpha_i(t)$ is determined by the associated photon-number-dependent pulled resonator frequency $\tilde{\omega}_{r,i}(|\alpha|^2)$ for the ith state with the equation of motion [19]

$$\dot{\alpha}_i = -i[\tilde{\omega}_{r,i}(|\alpha_i|^2) - \omega_d]\alpha_i - \kappa\alpha_i/2 - i\varepsilon_d/2. \tag{B6}$$

We discuss how to extract the functional form of $\tilde{\omega}_{r,i}(|\alpha|^2)$ in Appendix D. Our dynamical simulations are performed by first solving Eq. (B6) and then using the result to solve the Schrödinger equation under Eq. (B2).

Importantly, when part of the qubit population transitions to another state under a multiphoton resonance, the system evolves into an entangled transmon-resonator state that involves multiple $\alpha_i(t)$. The resonator state then becomes highly nonclassical, highlighting a key limitation of the semiclassical treatment. However, the resonator evolution can still be approximated by considering the dynamics of independently driven oscillators, each associated with a distinct transmon state [19]. Therefore, even above the ionization critical photon number, Eq. (B6) accurately describes the dynamics of the resonator associated with the ith transmon state. By carefully choosing $\tilde{\omega}_{r,i}(|\alpha|^2)$, we compute the resonator dynamics associated with the state population that remains in the initial qubit state throughout the readout process; see Appendix D. This allows us to investigate the dynamics of measurement-induced transitions at multiple critical photon numbers for a given initial qubit state.

Appendix C: Parameter fit with higher-order harmonics

The transmon Hamiltonian for a multiharmonic Josephson potential is given by Eq. (2) in the main text. It has been shown that higher-order harmonics, E_{Jm} for $m > 1$, must be considered to accurately describe the energies and charge dispersion of the transmon states beyond the qubit subspace [23].

The parameters $(E_C, E_{J1}, E_{J2}, E_{J3}, g, \omega_r)$ of Eq. (B1) for device B are fitted to spectroscopy data by minimizing the loss function

$$
\begin{aligned}
f = & \sum_{i=1}^{3} |\omega_{0i,n_g=0}^{\text{model}} - \omega_{0i,n_g=0}^{\text{exp}}|/i \\
& + \sum_{i=2}^{3} |\omega_{0i,n_g=0.5}^{\text{model}} - \omega_{0i,n_g=0.5}^{\text{exp}}|/i \\
& + \sum_{i=0}^{1} |\omega_{r,i}^{\text{model}} - \omega_{r,i}^{\text{exp}}|
\end{aligned} \tag{C1}
$$

using the Sequential Least Squares Programming optimization algorithm. Here, the ω_{0i} are the qubit transition frequencies between states 0 and i, and $\omega_{r,i}$ is the pulled resonator frequency corresponding to transmon state i. The model frequencies, $\omega_{0i}^{\text{model}}$ and $\omega_{r,i}^{\text{model}}$, are obtained from numerical diagonalization of Eq. (B1). The experimental qubit transition frequencies, ω_{0i}^{exp}, are measured in a Ramsey experiment at $n_g = 0$, in which transition frequencies of both parity are probed due to rapid quasiparticle tunneling events. The experimental pulled resonator frequencies, $\omega_{r,i}^{\text{exp}}$, are measured from the resonator response. The factor $1/i$ ensures that a larger weight is given to transitions involving lower-energy transmon states, since the quantities $\omega_{0i}^{\text{exp}}/i$ are all roughly measured to a precision of $\sim 0.1\,\text{MHz}$. Note that we only include the transition frequency ω_{10} at $n_g = 0$ in the cost function, owing to its negligible charge dispersion. To avoid overfitting, harmonics E_{Jm} of order $m \geq 4$ are set to zero, ensuring that the number of fitted parameters remains smaller than the number of measured frequencies.

The resulting fit parameters are shown in Table I. The first row presents the parameters fitted to the multiharmonic model. The rapid decay of the Josephson energies with increasing index m justifies the approximation of neglecting harmonics with $m \geq 4$. The second row presents the parameters fitted to the conventional single-harmonic transmon model. Significant differences in the fit parameters are observed between the two models, notably a change in E_J/E_C from 40.2 to 43.5.

To investigate the origin of the higher-order harmonics in our device, we fit the E_{Jm} to a model in which they arise from a stray inductor with inductive energy E_L in series with the Josephson junction; see the Supplementary Information of Ref. [23, 37]:. In the limit where $E_J/E_L \ll 1$, the higher harmonics E_{Jm} are then related to the Josephson and inductive energies by

$$E_{J1} \approx E_J \left[1 - \frac{1}{8}\left(\frac{E_J}{E_L}\right)^2 + \frac{1}{192}\left(\frac{E_J}{E_L}\right)^4 \right], \tag{C2a}$$

$$E_{J2} \approx E_J \left[-\frac{1}{4}\left(\frac{E_J}{E_L}\right) + \frac{1}{12}\left(\frac{E_J}{E_L}\right)^3 - \frac{1}{96}\left(\frac{E_J}{E_L}\right)^5 \right], \tag{C2b}$$

$$E_{J3} \approx E_J \left[\frac{1}{8}\left(\frac{E_J}{E_L}\right)^2 - \frac{9}{128}\left(\frac{E_J}{E_L}\right)^4 \right]. \tag{C2c}$$

Fitting our data to this model yields $E_J/2\pi = 8.693\,\text{GHz}$ and $E_L/2\pi = 284.2\,\text{GHz}$, corresponding to a linear inductance of $L = 0.575\,\text{nH}$. We expect a geometric inductance in that order of magnitude for that device geometry (see [23] supplementary). The third row of Table I shows the values of the higher-order harmonics and of the other parameters resulting from this fit. We note that the obtained parameters are in close range to the multiharmonic model ones, as is further discussed in Appendix H.

Appendix D: Floquet branch analysis

This section describes the Floquet branch analysis, a procedure for the identification of the critical photon numbers at which population is expected to leak outside the qubit subspace during readout [22].

When $\kappa \ll \omega_d$, the effective drive amplitude $\varepsilon_t(t) = 2g\sqrt{\bar{n}_r(t)}$ in Eq. (1) varies on a timescale much longer than the period of the drive, $T = 2\pi/\omega_d$. Thus, the Hamiltonian is approximately periodic at any given time, yielding an instantaneous Floquet spectrum at that time [38]. Starting from $\varepsilon_t = 0$ at time $t = 0$, the drive amplitude is increased by finite increments $\delta\varepsilon_t$. At each increment, the Floquet modes $|\phi[\varepsilon_t]\rangle$ and quasienergies $\epsilon[\varepsilon_t]$ are obtained by diagonalizing the one-period propagator over one period of the drive,

$$\hat{U}(t+T,t)\,|\phi(t)\rangle = e^{-i\epsilon T}\,|\phi(t)\rangle\,. \tag{D1}$$

The Floquet branch analysis classifies the modes and quasienergies into Floquet branches. At zero drive amplitude, the Floquet modes are just the bare transmon states, $|\phi_i[0]\rangle = |i\rangle$. The Floquet branch B_i associated with state $|i\rangle$ is constructed from the bare states as follows. The drive amplitude is progressively increased in increments of $\delta\varepsilon_t = 5\,\text{MHz}$. For each amplitude ε_t, the next Floquet mode $|\phi[\varepsilon_t]\rangle$ and associated quasienergy $\epsilon[\varepsilon_t]$ of the branch are chosen by maximizing the overlap

$$\big|\big\langle \phi[\varepsilon_t] \big| \phi_i[\varepsilon_t - \delta\varepsilon_t] \big\rangle\big|^2. \tag{D2}$$

The resulting Floquet branches for the multiharmonic model parameters of device B, see Appendix C, are shown in Fig. 6. Panel (a) shows the quasienergies of the Floquet branches, and panel (b) shows the average transmon population of the Floquet modes, $N_{t,i} = \sum_j j|\langle j|\phi_i(0)\rangle|^2$. Both quantities are plotted as a function of the average photon number $\bar{n}_r = (\varepsilon_t/2g)^2$. At specific photon numbers, resonances between the quasienergies of different branches lead to significant hybridization of the Floquet modes. This results in avoided crossings of the quasienergies in panel (a) and in a swapping of the transmon populations of the Floquet branches in panel (b). The avoided crossings of the ground and excited state branches allow us to identify the Floquet critical photon numbers for readout, which are indicated by the dotted vertical lines.

Model	$E_C/2\pi$ (MHz)	$E_{J1}/2\pi$ (GHz)	E_{J1}/E_C	E_{J2}/E_{J1}	E_{J3}/E_{J1}	$\omega_r/2\pi$ (GHz)	$g/2\pi$ (MHz)
Multiharmonic	216.6	8.718	40.2	-0.768 %	0.0398 %	7.04767	186.5
Conventional	205.6	8.948	43.5	0	0	7.04765	181.9
Stray inductance	217.4	8.694	40.0	-0.765 %	0.0117 %	7.04805	180.7

Table I. Fitted parameters for device B.

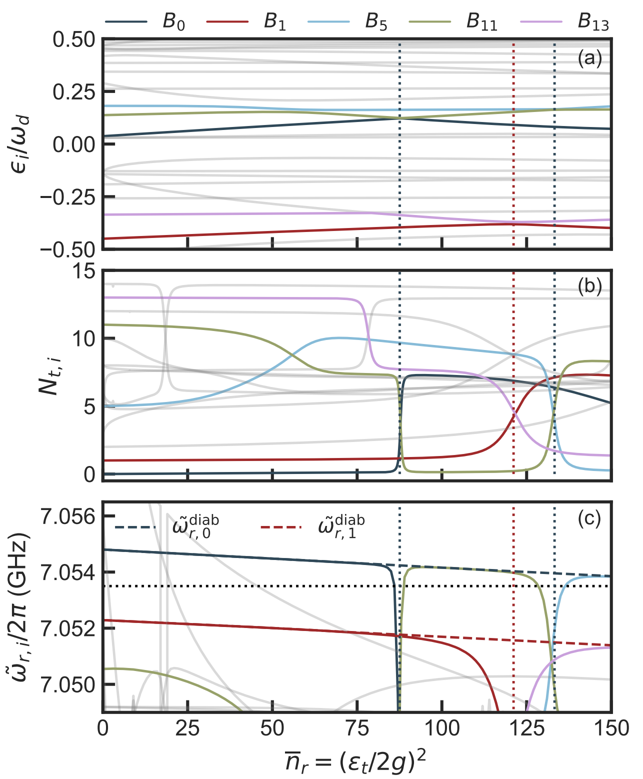

Figure 6. **Floquet branch analysis of device B.** (a) Floquet quasienergies, (b) average population of the Floquet modes, and (c) photon-number-dependent resonator frequency $\tilde{\omega}_{r,i}(\bar{n}_r)$ as a function of the average photon number $\bar{n}_r = (\varepsilon_t/2g)^2$ for $n_g = 0.23$. The dotted vertical lines indicate multiphoton resonances for the ground (blue) and excited (red) qubit states. In (c), $\tilde{\omega}^{\rm diab}_{r,0}$ (blue dashed line) and $\tilde{\omega}^{\rm diab}_{r,1}$ (red dashed line) are the pulled resonator frequencies obtained by diabatically tracking the qubit branches. The dotted black line indicates the value of ω_d. Branches B_0, B_1, B_5, B_{11}, and B_{13} are highlighted in color.

Note that multiple critical photon numbers can be extracted for each qubit state by diabatically tracking the branches, as explained further below.

Because the increment $\delta\varepsilon_t$ is chosen to be relatively small, the tracking emulates an adiabatic increase in the photon number $\bar{n}_r$ as a function of time. Such an adiabatic evolution through an avoided crossing results in full population transfer at that avoided crossing. To quantitatively understand the effect of the resonances on measurement-induced transitions, however, it is crucial to examine how they affect the dynamical processes during readout. During this process, the average resonator photon number $\bar{n}_r$ can increase more or less rapidly, as discussed in Appendix F. At low photon number, the state population mostly follows the initial branch. When the photon number reaches an avoided crossing of the quasienergies, the transmon population splits between the branches following a Landau-Zener process [39]. The transition can be more or less diabatic depending on the rate of change of $\bar{n}_r$ [19]. The probability of staying on the initial branch, and thus of exiting the computational subspace, is $1-P_{\rm LZ}$, where $P_{\rm LZ} = \exp(-\pi\Delta^2_{\rm ac}/2v)$ is the Landau-Zener transition probability. Here, $\Delta_{\rm ac}$ is the energy gap at the avoided crossing and $v(\varepsilon_t)$ is the speed of passage through the resonance [40–43]. Thus, larger gaps and lower crossing speeds both increase the probability of the measurement-induced transitions.

Here, we aim to track the qubit population beyond the first crossing to capture multiple critical photon numbers. In Fig. 6(b), for example, the population initialized in B_0 can transition to higher-energy levels at $\bar{n}_r \approx 88$. However, if the population diabatically transfers to B_{11}, which is 0-like after the crossing, the next critical photon number is found at $\bar{n}_r \approx 133$ due to an avoided crossing with B_5. To diabatically track the state i and identify all such critical photon numbers for that initial state, we start from branch B_i at zero photon number and gradually increase $\bar{n}_r$. When an avoided crossing between B_i and another branch B_j is reached, the tracked branch switches to B_j, which becomes more i-like beyond the crossing. Then, B_j is tracked until the next avoided crossing with another branch B_k. The Floquet critical photon numbers shown in Fig. 4(b) correspond to all photon numbers at which the tracked branch is changed.

Even though the semiclassical model does not explicitly include the resonator, the Floquet analysis nevertheless enables the computation of the pulled resonator frequencies for each qubit state and for each resonator photon number. To do so, we assign to each Floquet branch B_i an effective nonlinear oscillator with photon-number dependent frequency $\tilde{\omega}_{r,i}(\bar{n}_r)$ given by

$$\tilde{\omega}_{r,i}(\bar{n}_r) = \omega_r + \epsilon_i(\bar{n}_r+1) - \epsilon_i(\bar{n}_r), \tag{D3}$$

where $\epsilon_i(\bar{n}_r)$ is the Floquet quasienergy of branch B_i computed at the effective drive amplitude $\varepsilon_t = 2g\sqrt{\bar{n}_r}$. The frequencies obtained in this way are very close to those obtained from the diagonalization of the full transmon-resonator Hamiltonian [22]. This method thus accounts for nonlinear effects at high photon numbers while remaining computationally more efficient than full diagonalization. The effective oscillator frequencies of the Floquet branches are shown in Fig. 6(c). They display significant nonlinear photon number dependence around the critical photon numbers. To dynamically follow the population in the qubit-like branch, we define $\tilde{\omega}_{r,i}^{\mathrm{diab}}$, the effective oscillator frequency obtained by diabatically tracking branch B_i as described above. Across the relevant range in photon number, the pulled resonator frequencies $\tilde{\omega}_{r,0}^{\mathrm{diab}}$ and $\tilde{\omega}_{r,1}^{\mathrm{diab}}$ vary approximately linearly with $\bar{n}_r$, with slopes $K_0/2\pi \approx -6.6\,\mathrm{kHz}$ and $K_1/2\pi \approx -5.5\,\mathrm{kHz}$ corresponding to the resonator self-Kerr nonlinearities. The diabatic oscillator frequencies for branches B_0 and B_1 are shown as dashed colored lines in panel (c).

The choice to follow the resonator dynamics associated with the qubit-like branch stands on the assumption that most of the state population does not suffer from measurement-induced transitions and therefore remains in the initial branch for the whole readout duration. However, this approximation does not always hold. For example, at large photon numbers, measurement-induced transitions can sometimes lead to population transfers exceeding 50% due to the presence of large avoided crossing gaps in the quasienergy spectrum. Despite this limitation, this choice allows us to model the resonator dynamics for the remaining qubit population, ensuring accurate modeling of the measurement-induced transitions even beyond the first threshold. Hence, the time-dynamics simulations correctly identify many photon numbers at which we observe drops in the experimental qubit state survival probability. However, with this approach, we expect the modeling of the resonator dynamics to be inaccurate for the state population transferred to high-energy states, for which the photon-number dependent frequency $\tilde{\omega}_{r,i}$ can be significantly off-resonant from that of the qubit-like branch, $\tilde{\omega}_{r,i}^{\mathrm{diab}}$. Therefore, we do not expect the simulations to quantitatively reproduce the population transfer from higher-energy states to the qubit-like state during the resonator ramp-down. In Fig. 4, discrepancies between the qubit state survival probability for the experimental data in panel (b) and the time-dynamics simulations in panel (c) are attributed to this source of error.

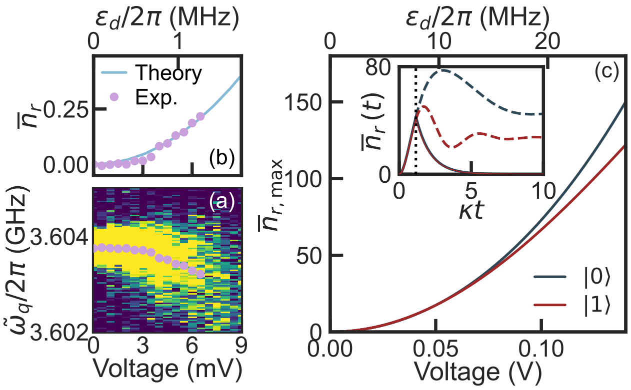

Figure 7. **Photon number calibration for device B.** (a) Experimentally measured qubit frequencies as a function of applied voltage (purple dots). The background shows the measured spectroscopic response for each voltage. (b) Steady-state photon number extracted from Eq. (E1) as a function of voltage in the linear regime (purple dots), and computed by solving Eq. (B6) as a function of the resonator drive amplitude ε_d (light blue line). The curves are made to correspond by rescaling the applied voltage, yielding a linear relation between the voltage and ε_d. (c) Maximum average photon number obtained by solving Eq. (B6) as a function of applied voltage for a pulse duration of 200 ns when the qubit is initialized in the ground state (blue) or excited state (red). The inset shows the time evolution of $\bar{n}_r$ for $\varepsilon_d/2\pi = 15\,\mathrm{MHz}$. The solid lines show the evolution of the photon number when the drive is turned off after 200 ns (dotted vertical line) for the qubit initialized in the ground state (blue) or excited state (red). The dashed lines show the evolution of the photon number if the drive is not turned off after 200 ns.

Appendix E: Nonlinear photon number calibration

Here, we describe the procedure used to calibrate the photon number of device B as a function of the experimentally applied voltage. At low photon numbers, the qubit frequency is ac-Stark shifted proportionally to the average resonator photon number $\bar{n}_r$,

$$\tilde{\omega}_q(\bar{n}_r) = \omega_q + \chi \bar{n}_r. \tag{E1}$$

Here, $\chi = \chi_1 - \chi_0$ is the full dispersive shift, with χ_0 and χ_1 the dispersive shifts for the ground and excited states, respectively. In this linear regime, the extracted shifted frequencies $\tilde{\omega}_q$ can be converted into a photon number using the measured χ shift and Eq. (E1). This in turn allows us to convert the applied voltage into a photon number through the observed relationship between $\tilde{\omega}_q$ and the voltage. Figure 7(a) shows the experimentally measured qubit frequency as a function of the applied voltage (purple dots). The values of χ_0 and χ_1 are measured separately and subtracted to yield the total dispersive shift $\chi/2\pi = -2.5\,\mathrm{MHz}$. This value yields the relationship between photon number and applied voltage shown as the purple dots in Fig. 7(b).

At larger photon numbers, the linear calibration is not expected to be accurate [44]. To calibrate the photon number in the nonlinear regime, we account for the nonlinear dispersion extracted in Appendix D (here dominated by the resonator self-Kerr). We first use the calibration in the linear regime to establish the relationship of the resonator drive ε_d to the experimentally applied voltage. To do so, we compute the steady-state photon number when the qubit is in the ground state, $\bar{n}_r \equiv |\alpha_0|^2$, as a function of the drive amplitude ε_d. We do this by solving Eq. (B6) using the (diabatic) nonlinear dispersion $\tilde{\omega}_{r,0}^{\mathrm{diab}}(\bar{n}_r)$ for $i = 0$ and the experimental drive frequency ω_d. The result is shown in Fig. 7(b). By merely rescaling the experimentally applied voltage by a constant factor, we are able to match the experimentally calibrated photon numbers (purple dots) to the theoretical values (blue line) in the linear regime. This establishes that the relationship between the voltage and ε_d is linear. This linear relation is expected to hold because the nonlinearity of the measurement chain is expected to be hold within the explored voltages.

Using the characterized linear relationship between the applied voltage and ε_d, we solve Eq. (B6) to yield the average photon number at any given integration time. Figure 7(c) shows the maximum photon number for a pulse duration of 200 ns as a function of the applied voltage. The blue line shows the result when the qubit is initialized in the ground state with dispersion $\tilde{\omega}_{r,0}^{\text{diab}}(\bar{n}_r)$, and the red line shows the result when the qubit is initialized in the excited state with dispersion $\tilde{\omega}_{r,1}^{\text{diab}}(\bar{n}_r)$. The upper axis shows the corresponding drive amplitude ε_d. At large voltages, the resonator photon number reaches considerably larger values when the qubit is in the ground state. This occurs because the drive frequency ω_d is set between the pulled resonator frequencies for the two qubit states and because the self-Kerr nonlinearity is negative. For that reason, the frequency $\tilde{\omega}_{r,0}^{\text{diab}}(\bar{n}_r)$ becomes more resonant with ω_d at large photon numbers; see Fig. 6(c). By contrast, $\tilde{\omega}_{r,1}^{\text{diab}}(\bar{n}_r)$ becomes more off-resonant with ω_d at large photon numbers. The inset of Fig. 7(c) shows the time-dependent photon number for $\varepsilon_d/2\pi = 15\,\text{MHz}$ when the qubit is initialized in the ground state (blue line) or in the excited state (red line). The vertical dotted line indicates the experimental pulse duration $t = 200\,\text{ns}$. We also show what the evolution of the photon number would be for the ground state (dashed blue line) and for the excited state (dashed red line) if the drive were not turned off beyond 200 ns. Since $\kappa \sim |\omega_{r,i}^{\text{diab}} - \omega_d|$ for both initial qubit states, the oscillator is in the underdamped regime and the photon number oscillates in time. Nevertheless, there are no oscillations in the photon number within the experimental readout pulse duration of 200 ns. We note that this regime is different from the one investigated in Ref. [22], where it was assumed that $\kappa \gg |\omega_{r,i}^{\text{diab}} - \omega_d|$. Calibrating the photon number in the appropriate regime is crucial to accurately model the resonator dynamics and identify the critical photon number.

Finally, we note that we only calibrate the photon number for one value of n_g since the diabatic dispersions $\tilde{\omega}_{r,i}^{\text{diab}}(\bar{n}_r)$ is largely insensitive to n_g for the computational states. These dispersions also ignore the effect of the n_g-sensitive multiphoton resonances (see Appendix D). Therefore, we expect the calibration to be approximately the same for all n_g.

Appendix F: Dynamics of the driven transmon

In this section, we describe the time dynamics simulations of the driven transmon used to study the dynamics of qubit ionization in device B. The transmon state is first initialized in the ground or excited state, $|\psi(t_0)\rangle = |i\rangle$ with $|i\rangle = |0\rangle$ or $|1\rangle$, respectively. It is then evolved by solving the Schrödinger equation for the effective time-dependent Hamiltonian in Eq. (1), with solution at time t given by $|\psi_i(t)\rangle = \hat{U}(t, t_0)\,|i\rangle$. The time-dependent average photon number $\bar{n}_r(t) = |\alpha_i(t)|^2$, which determines the effective drive amplitude $\varepsilon_t(t) = 2g\sqrt{\bar{n}_r(t)}$ in Eq. (1), is computed from Eq. (B6) with initial qubit state i. The resonator drive ε_d is switched on at the initial time, leading to a gradual increase of $\bar{n}_r(t)$. The drive is then turned off after 200 ns, after which the resonator gradually empties on a timescale of $1\,\mu\text{s} \approx 6/\kappa$. We compute the Floquet basis $|\phi_i[\varepsilon_t(t)]\rangle$ associated with the instantaneous value of $\varepsilon_t(t)$. The projection of the time-evolved state on that instantaneous Floquet basis then gives the time-dependent probability $P(j|i)$ of transitioning from the initial ith branch to the final jth branch:

$$P(j|i) = |\langle \phi_j[\varepsilon_t(t)]|\psi_i(t)\rangle|^2. \tag{F1}$$

In particular, the quantity $1 - P(i|i)$ describes the final population transfer out of the initial Floquet branch at the final time $t = 1.2\,\mu\text{s}$ and is thus a proxy for the experimentally observed probability of measurement-induced transitions (assuming that the two low-power readout pulses cause negligible state transitions).

Whenever the photon number $\bar{n}_r$ approaches an avoided crossing in the Floquet quasienergies, the population generically splits between the two associated Floquet branches. These populations subsequently interfere in a way that affects the population transfer at the final time. Experimentally, however, rapid decoherence of such superpositions is expected since the resonator pulls $\tilde{\omega}_r$ of the Floquet branches are substantially different; see Fig. 6(c). Any fluctuation in the photon number due to, e.g., quantum fluctuations, leads to fluctuations in the quasienergy difference between the branches and thus to dephasing. The aforementioned interference effects, which are a feature of our fully coherent semiclassical model, are thus not expected to be observed in practice. To roughly mimic this unavoidable dephasing between Floquet branches, the coherences in the Floquet basis are manually set to zero at the end of the ramp up at $t = 200\,\text{ns}$. The diagonal elements of this decohered state are then evolved separately and coherently during the ramp down. The final transition probability is reconstructed by summing the transition probabilities for all possibilities:

$$P(i|i) = \sum_j P_{\text{down}}(i|j) P_{\text{up}}(j|i). \tag{F2}$$

Here, $P_{\text{up}}(j|i) = |\langle \phi_j[\varepsilon_t(t_{\text{up}})]|\psi_i(t_{\text{up}})\rangle|^2$ is the population transferred from the prepared ith transmon state to the jth Floquet mode after a ramp-up of $t_{\text{up}} = 200\,\text{ns}$. The quantity $P_{\text{down}}(i|j) = |\langle \phi_i[\varepsilon_t(t_f)]|\hat{U}(t_f, t_{\text{up}})|\phi_j[\varepsilon_t(t_{\text{up}})]\rangle|^2$ is the transition probability from the state initialized in the jth Floquet mode at the time t_{up} back to the ith

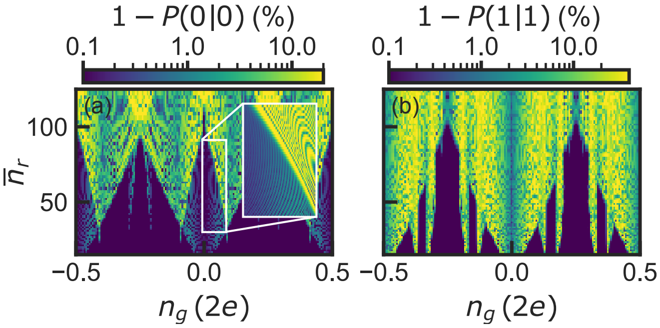

Figure 8. **Measurement-induced transitions without coherence collapse in the semiclassical dynamics.** The transition probability is shown as a function of gate charge and average photon number when initializing the qubit in (a) the ground state and (b) the excited state. The inset highlights the presence of fast oscillations in the transition probability.

Floquet mode at the end of the ramp-down at the final time $t_f = 1.2\ \mu$s. In the bottom row of Fig. 4(b) of the main text, we plot the quantity $1-P(i|i)$ computed from Eq. (F2) for various values of the drive amplitude ε_d and of the offset charge n_g.

To illustrate this point, Fig. 8 shows the probability of state transition at the final time *without* the artificial collapse of the coherence starting in (a) the ground state and (b) the excited state. While the results first appear to be very coarse, the inset reveals the presence of very sharp oscillations as a function of both n_g and $\bar{n}_r$. The absence of oscillations in the experimental data is further confirmed by the results of the quantum simulations outlined below. However, we do not present the full sweep over the gate charge and drive power due to the significant time and computational resource requirements.

To highlight the dynamical nature of the transition process, we plot the transition probability as a function of time in Fig. 9(a) for different values of n_g; the gate charge; see the solid lines. Figure 9(b) shows the average photon number as a function of time, with the horizontal dashed lines showing the critical photon numbers obtained from the Floquet analysis for the same values of n_g as in (a). The results highlight the importance of considering the effect of both the photon number ramp-up and ramp-down on the final transition probability, with sharp variations of the probability observed when the critical photon number is reached during both phases. The qubit population transitions at later or earlier times depending on the charge value, which is due to resonances occurring at critical photon numbers that depend on n_g. Note that the probabilities always peak near 50% at the critical photon numbers, as the Floquet modes are in an equal superposition of the qubit states at that point.

In addition to comparing with the experimental data, we further validate the accuracy of the predictions of the semiclassical model by computing the time dynamics of the full quantum model described by Eq. (B1), which

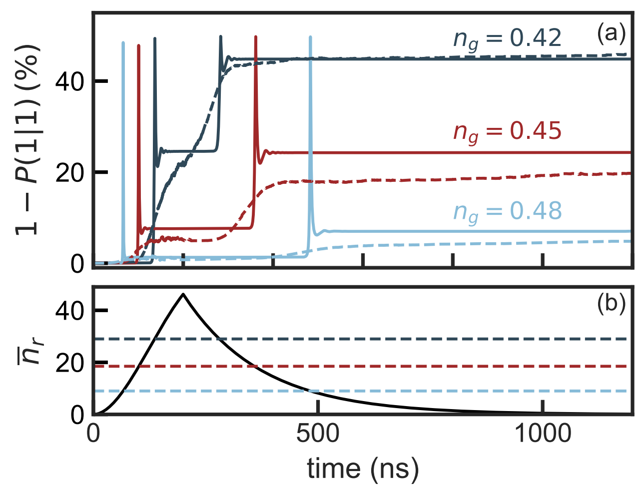

Figure 9. **Temporal profile of measurement-induced transitions in simulations of device B.** (a) Probability to transition out of the qubit excited state branch as a function of time when solving the dynamics of the semiclassical model (solid lines) and of the quantum model (dashed lines) for three different values of the gate charge. (b) Average photon number calculated from the semiclassical model for a drive amplitude $\varepsilon_d/2\pi = 16\,$MHz turned on for 200 ns when initializing the qubit in the excited state. The dashed lines correspond to the Floquet critical photon numbers for the same values of the gate charge as in (a).

evolves under the following Lindblad master equation,

$$\partial_t\hat{\rho} = -i[\hat{H}_{tr} - i\varepsilon_d \sin(\omega_d t)(\hat{a}-\hat{a}^\dagger), \hat{\rho}] + \kappa\mathcal{D}[\hat{a}]\hat{\rho}. \quad \text{(F3)}$$

Here, ε_d and ω_d are the drive amplitude and frequency, κ is the single-photon loss rate of the resonator, and $\mathcal{D}[\hat{a}]\hat{\rho}$ is the usual Lindblad dissipator. The simulated Hilbert space is large because of the high resonator photon number and the necessity of considering many transmon states above the cosine potential, which makes the simulations computationally intensive and limits the ability to perform extensive parameter sweeps. Rather than simulating the full evolution, we evolve individual realizations of 500 quantum trajectories, which significantly accelerates the calculations. Instead of sweeping over the entire parameter range, we only investigate the dynamics for $\varepsilon_d/2\pi = 16\,$MHz and the same three values of gate charge used in Fig. 9(a). The state is initialized in the dressed excited qubit state at zero photon number.

At each moment, we project the evolved state onto the set of states defined by the diabatic tracking of the full quantum branch B_1, which is constructed using the branch analysis formalism of Ref. [19]. This quantity defines the probability that the population remains in the initial state at each moment, in a similar spirit to the quantity defined in Eq. (F1) for the semiclassical dynamics. The results are shown as a function of time in Fig. 9(a) for $n_g = \{0.42, 0.45, 0.48\}$. In all three cases, the quantum time-dynamics shows that a sharp increase in state transition probability occurs at the same photon numbers and times as in the semiclassical model. Furthermore, both models show the effect of the photon number ramp-up and ramp-down on state transitions, with an increase in population transfer observed around the critical photon number during both phases. Note that the increase of the transition probability is smoother for the quantum model than the semiclassical one due to the quantum photon number fluctuations in the resonator. Furthermore, relatively good agreement in the final transition probability is observed between the quantum and semiclassical models. The agreement between the results of both models validates the use of the semiclassical model to predict both the onset and the probability of demolition, with the added benefit of being much more computationally efficient.

Appendix G: Impacts of charge-sensitive states on measurement-induced transitions

In this section, we investigate the role of high-energy states in the charge dependence of measurement-induced transitions. The charge dispersion of the transmon increases exponentially with the level index [3]. This impacts the resonances that involve these excited states. Figure 10(a) shows the gate-charge dependence of the Floquet critical photon numbers for measurement-induced transitions from the qubit ground state to excited states i in device B. All resonances involve very high-energy states, such as 8, 9, and 11. These states lie above the cosine potential well and exhibit charge dispersion on the order of 1 GHz. As expected, the higher the level index, the stronger the dependence on n_g, with the resonance involving 11 showing the most pronounced dependence. To emphasize the role of higher-energy states in the charge-dependence of state transitions, Fig. 10(b) shows the quasienergy spectrum for $n_g = 0.01$ (solid lines) and $n_g = 0.11$ (dashed lines). At low photon number, the quasienergy of branch B_0 does not show a dependence on n_g due to the negligible charge dispersion of the ground state level in the transmon regime, which is clearly not the case for B_8 and B_9. When $n_g = 0.01$, a crossing between B_0 and B_9 is observed around $\bar{n}_r \approx 95$. However, when $n_g = 0.11$, an earlier crossing with B_8 takes place at $\bar{n}_r \approx 40$, while the resonance with B_9 does not exist. The resonance between B_0 and B_8 is also present when $n_g = 0.01$, but at a smaller photon number $\bar{n}_r \approx 10$. The interaction strength in this case is not sufficient to induce significant hybridization of the states, which prevents the formation of an avoided crossing for the selected drive increment $\delta\varepsilon_t = 5\,\mathrm{MHz}$.

Even deeper in the transmon regime, the onset of measurement-induced transitions is expected to remain charge-dependent. Indeed, while the charge sensitivity of the qubit states decreases exponentially with E_J/E_C, the higher-energy levels involved in the resonances do not benefit from this protection. Figure 11(a) shows the charge-dependent Floquet critical photon numbers as a function of readout frequency for a deep transmon with $E_J/E_C = 100$. The critical photon numbers are shown as colored dots for both the ground and excited states, with the colors indicated six different values of the gate charge. The area of the dots is proportional to the size of the quasienergy gap. Strong dependence of the position of the resonances on the gate charge is observed. In some range of ω_d, the critical photon numbers are on average larger. However, there are still resonances occurring at lower photon numbers for specific values of n_g, even though we consider only six values of n_g. Therefore, selecting a readout frequency for which variations of the charge do not limit the average onset of measurement-induced transitions is very difficult, if not impossible. In contrast, Fig. 11(b) shows the same critical photon numbers as in Fig. 11(a), but for a single value of the charge, $n_g = 0$. In this case, the distribution of the resonances is much less dense, and one can easily identify values of ω_d for which the onset of transitions is pushed to large photon numbers. This suggests that the critical photon numbers can on average be increased with charge stabilization even deep in the transmon regime, which could prove beneficial to dispersive readout performance.

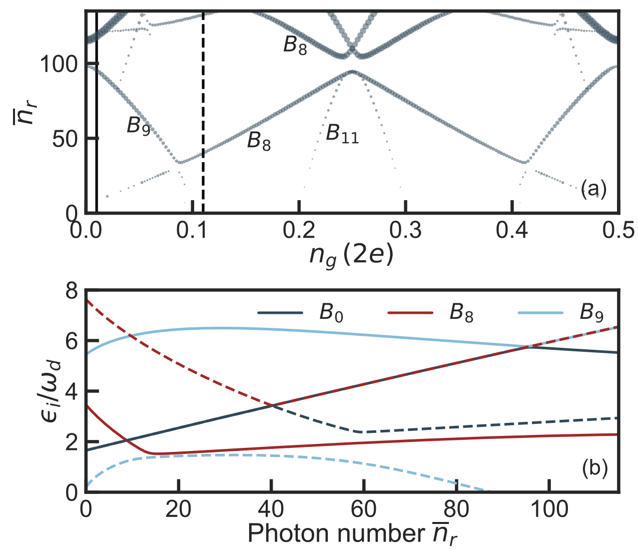

Figure 10. **Investigation of the role of higher-energy states in measurement-induced transitions in device B.** (a) Floquet critical photon numbers for resonances between the ground state and excited states as a function of gate charge. Branches involved in the resonances are identified on the plot. (b) Quasienergy of branches B_0, B_8 and B_9 taken at $n_g = 0.01$ (solid lines) and $n_g = 0.11$ (dashed lines) as a function of average photon number. The vertical lines in (a) serve to guide the eye.

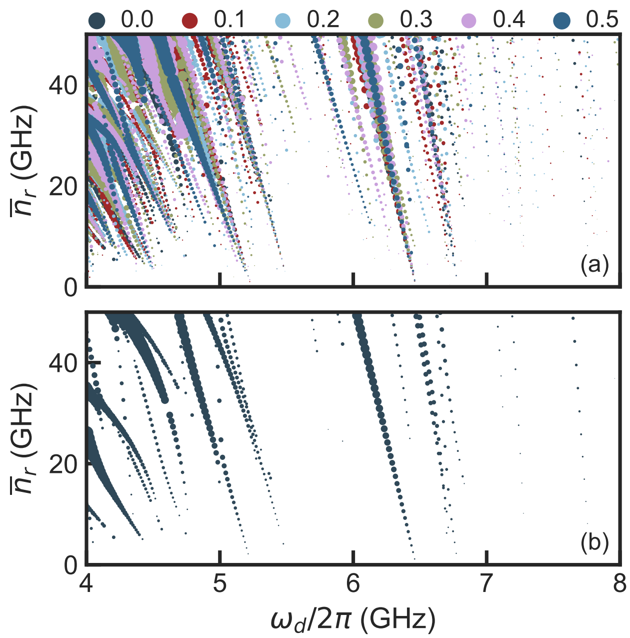

Figure 11. **Measurement-induced transitions in the deep transmon regime with $E_J/E_C = 100$ and $\omega_q/2\pi = 3.61\,\mathrm{GHz}$.** Floquet critical photon numbers involving the qubit computational states as a function of ω_d for (a) 6 different values of offset charge linearly spaced between $n_g = 0$ and $n_g = 0.5$ (see legend) and (b) for $n_g = 0$ only. I changed the plot here. Let me know what you prefer between image_deep_transmon and image_deep_transmon_2.

Appendix H: Comparison of the results with and without inclusion of higher-order harmonics

As discussed in Appendix C, we fit both the conventional transmon model and the higher-order harmonics model to the measured spectroscopy data of device B. To avoid over fitting only the first and second transmon transitions are fitted to the conventional model. Moreover, the time dynamics of the semiclassical model is computed using the parameters fitted to both the conventional transmon and higher-order harmonics models. The comparison is shown in Fig. 12 for the ground state (left column) and the excited state (right column). Panels (a-b) reproduce the results presented in the main text, see Fig. 4(b), namely the experimental data and the semiclassical time-dynamics results with the parameters fitted to the higher-harmonics model. Panel (c) shows the semiclassical time-dynamics results for the conventional model parameters. The latter do not align with the experimental data shown in (a). For example, significative transitions out of the qubit ground state is expected around $n_g \approx 0$ at low photon numbers, which is not observed in the experimental data.

To make this comparison clearer, the Floquet critical photon numbers computed from the two sets of parameters are displayed above the experimental data in panel (a). Significant mismatch is observed between the offset-charge dependent features in the experimental data and the critical photon numbers for the conventional transmon model (black circles). This is in sharp contrast with the excellent agreement between the experimental features and the critical photon numbers for the higher-harmonics model (red circles). The disparity between the theoretical predictions of the two models can be explained by the significant variation in the ratio E_{J1}/E_C, as was discussed in Ref. [23]. This ratio has a considerable impact on the energy and dispersion of the transmon's high-energy states involved in measurement-induced transitions. These results support the presence of higher-order harmonics in the transmon Hamiltonian and highlight the need to carefully model the high-energy sector of the transmon, and potentially of other Josephson-junction based qubits, in order to accurately reproduce the onset of measurement-induced state transitions.

We note that the results of the time dynamics using the parameters from the series inductance fit, which are listed in the third row of Table I, are very similar to those shown in Fig. 12(b). This is due to the fact that the parameters are in close range to those obtained from the higher-harmonics fit, see the first row of Table I. The largest relative variation of the parameters resides in the third-order harmonics, E_{J3}. However, with $E_{J3}/E_J < 0.1\%$, even relatively large variations of this parameter does not significantly impact neither the onset nor probability of demolition. Since the experimental results can be accurately reproduced with two sets of parameters that fall within the physical bounds of both the high-transparency channels in the junction [23] and the series inductance models with a realistic value of $L = 0.575\,\mathrm{nH}$ [23], our analysis does not provide further insight into the physical origin of the higher-order harmonics in the Hamiltonian. However, in the case of transmons with larger harmonics [23], investigating the charge-dependent onset of demolition could be used as a means of scanning the high-energy spectrum of the transmon. In this case, comparing the experimental results to the theoretical predictions from the different model could help elucidate the origin of these harmonics.

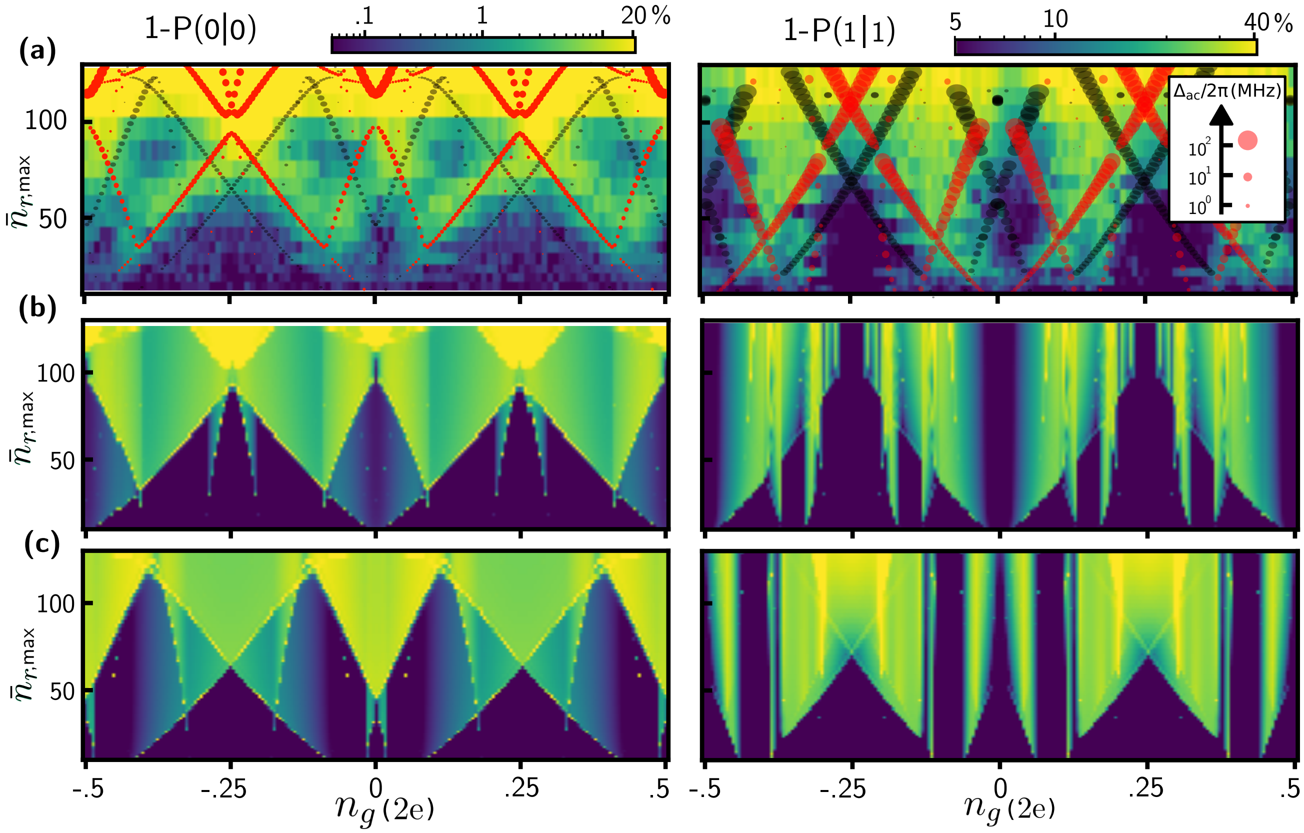

Figure 12. **Impact of higher-order harmonics in the modeling of device B on the transitions**. Measurement-induced transitions for the ground state (left column) and the excited state (right column) as a function of offset charge and maximal readout photon number. (a) Experimental data is shown in the background, with circles on top indicating the positions of avoided crossings in the Floquet quasienergy spectrum for the higher-harmonics model (red) and the conventional transmon model (black). The dot area is proportional to the gap size Δ_{ac}. (b-c) Semiclassical time dynamics results using the Hamiltonian parameters fitted to (b) the higher-harmonics model and (c) the conventional transmon model.